Revista Mexicana de Astronomía y Astrofísica, **47**, 385–399 (2011)

KINEMATICS FROM SPECTRAL LINES FOR AGN OUTFLOWS BASED ON TIME-INDEPENDENT RADIATION-DRIVEN WIND THEORY

J. M. Ramírez

Leibniz-Institut für Astrophysik Potsdam, Germany

Received 2011 January 17; accepted 2011 August 5

RESUMEN

Construimos un modelo de fotoionización dependiente de la velocidad para el absorbedor tibio de NGC 3783. Adoptando formas funcionales de la velocidad del flujo y su densidad del número de partículas con el radio, apropiadas para un viento acelerado por radiación, calculamos el nivel de ionización, la temperatura, el corrimiento Doppler y las profundidades ópticas de las líneas como función de la distancia. El modelo reproduce la relación observada entre la ionización del gas y el corrimiento del centroide de las líneas de absorción en NGC 3783. Este espectro requiere de la presencia de dos flujos: uno altamente ionizado responsable de las alas azules de las líneas de alto grado de ionización y al mismo tiempo las alas rojas de las líneas de menor grado de ionización; y uno de baja ionización que produce las alas azules de las líneas de oxígeno.

ABSTRACT

We build a bulk velocity-dependent photoionization model of the warm absorber of the Seyfert 1 galaxy NGC 3783. By adopting functional forms for the velocity of the flow and its particle density with radius, appropriate for radiation-driven winds, we compute the ionization, the temperature, the line Doppler shift, and the line optical depths as a function of distance. The model reproduces the observed relationship between the gas ionization and the velocity shift of the absorption line centroids in the X-ray spectrum of NGC 3783. The distribution of asymmetry seen in this spectrum requires the presence of two outflows: a higher ionization component responsible for the blue wings of the high ionization lines and the red wings of the low ionization oxygen lines, and a lower ionization flow that produces the blue wings of the oxygen lines.

Key Words: galaxies: Seyfert — quasars: absorption lines — quasars: individual (NGC 3783)

1. INTRODUCTION

X-ray (0.5–10 keV) *Chandra* spectra of type-I active galactic nuclei (AGN) often show the presence of absorption lines coming from H- and He-like ions of O, Ne, Mg, Si, S as well as from Fe XVII-Fe XXIII L-shell transitions. These lines are near the region of the bound-free absorption edges of O VII and O VIII at $\sim$0.8 keV, which are the hallmark of warm absorbers (George et al. 1998; Komossa 1999). In Seyfert 1 galaxies these absorption lines can be narrow (Seyfert 1 NALs) with full width at half maximum (FWHM) spanning $\sim$100–500 km s^{-1} (Kaspi et al. 2000), or broad (Seyfert 1 BALs) with FWHM $\sim$500–2000 km s^{-1} (Kaspi et al. 2001). The troughs of the lines are blue-shifted relative to rest frame of the host galaxy with velocities that go from several hundred to a few thousand km s^{-1} (Yaqoob et al. 2003), implying the presence of outflows that cover a wide range of velocities and ionization stages (Kaastra et al. 2000; Kaspi et al. 2002; Krolik & Kriss 2001; Różańska et al. 2006).

In Seyfert galaxies and quasars, absorption spectra show a range of ionization stages that arise from ionization parameters that span $\xi\sim$10–1000 erg cm s^{-1} (Kaspi et al. 2002). Simultaneous UV and X-ray observations may enhance this range even further (Shields & Hamann 1997; Gabel et al. 2005). The location of these absorbing material is uncertain. Models of X-ray absorbers in AGN place them in a wide range of distances from the central source, from winds originated at the accretion disk (Murray et al. 1995; Elvis 2000), out to the dusty ($\sim$1 pc) torus (Krolik & Kriss 2001) and beyond the narrow-line region (e.g., Ogle et al. 2000).

In the Seyfert galaxy NGC 3783 the 900 ks *Chandra* spectrum of Kaspi et al. (2002) allows the precise measurements of radial velocities and widths of the lines. It is seen that the velocity shift of lines from Fe XXIII-Mg XII covers a range of $\sim$60–600 km s^{-1} while the low-ionized lines Si XIII-O VII cover velocities $\sim$500–1000 km s^{-1} (see Figure 6 in Ramírez, Bautista, & Kallman 2005). The average velocity of the warm absorber outflow of NGC 3783 is around $\sim$500 km s^{-1}. The spectrum also reveals that the line profiles are asymmetric (Kaspi et al. 2002), in such a way that approximately 90% of the lines have extended blue wings. Such asymmetries were quantified by Ramírez et al. (2005). In terms of ionization, mostly high ionization species are seen in the short-wavelength portion of the spectrum $\sim$4–12 Å. Here, resonant lines from Fe XXIII, Fe XXII, Fe XXI, S XVI, S XV, Si XIV, and Mg XII cover ionization parameters ξ from $\sim$630 to $\sim$150 erg cm s^{-1}. The longer wavelengths of the spectrum, $\sim$10–20 Å, are dominated by lower ionization lines from Si XIII, Fe XVIII, Ne X, Mg XI, Fe XVII, Ne IX, O VIII, and O VII that span ionization parameters ξ from $\sim$125 erg cm s^{-1} down to $\sim$8 erg cm s^{-1}.

Thus, photoionization modeling shows that the observed spectrum is hardly explained by a single ionization parameter. Rather two or three components are needed, and this has been the subject of well-detailed studies (Krongold et al. 2003; Netzer et al. 2003; Krongold et al. 2005). In these papers two/three components in pressure equilibrium are enough to account for all the charge states seen in the spectra. At the start of these simulations, the ionization parameter is not kept constant throughout the cloud but made to vary in a self-consistent way. On the other hand, Steenbrugge et al. (2003) used a nearly continuous distribution of ionization parameters that spans three orders of magnitude. In reality both approaches do not need to be contradictory. We just have to look at the possibility of introducing species between the components proposed by Krongold et al. (2003); Netzer et al. (2003); Krongold et al. (2005); and this immediately leads us to the discussion of whether the material absorbing is clumpy or not. And this is in part the goal of the present work. We present both possibilities, continuous *vs* clumpy flows, with their physical implications.

Although there is no evident correlation between the ionization of the absorption species and the velocity shifts of lines (Kaspi et al. 2002), Ramírez et al. (2005) suggested the possibility for such relationship to exist, as the lines are consistent with being originated from an outward flowing wind. In that work a wind velocity law was adopted (Castor, Abbott, & Klein 1975), with an ionization fraction that goes as a power-law of the ionization parameter $q \sim \xi^{\eta}$ with $\eta > 0$ for all ξ and all lines. Further, $q \sim \xi^{\eta}$ and an optical depth of the form proposed by the SEI method from Lamers, Cerruti-Sola, & Perinotto (1987) were used to fit the lines in the spectrum and to study the possible relationship between the profiles and the expansion velocity of the flow.

Here, in this theoretical approach no analytical dependence of q with ξ is assumed, but it is computed self-consistently using the photoionization code XSTAR with modifications of the optical depth of the lines to work with an expanding outflow.

It is the aim of the present paper to further study the wind scenario for the warm absorber of NGC 3783 by modeling a photoionized wind flow and trying to reproduce the main features in the spectrum in terms of both equivalent widths and line profiles. The model consists of a spherically symmetric gas flow with velocity increasing with radius according to the wind velocity law of Castor et al. (1975). The microphysics of the plasma is then solved in detail along the wind, and radiative transfer is treated for the flowing plasma including Doppler shift effects on the emerging spectrum. This kind of approach has been used previously in studies of the ionization and thermal properties of O stars by Drew (1989), on cataclysmic variables by Drew & Verbunt (1985) and in an evaluation of absorption line profiles from winds in AGN by Drew & Giddings (1982).

Self-consistent hydrodynamic modeling of AGNs has been performed in the past (see e.g., Murray et al. 1995) who qualitatively predict the same β-velocity law, where $v(r) \sim (1 - r_0/r)^{\beta}$, as adopted here. However, these models did not include a detailed treatment of the thermal and spectral processes that lead to synthetic spectra.

The present paper is organized as follows: In § 2 we discuss the statistical significance of the X-ray lines under study. Later in § 3, we present the theoretical method we have used in this work. In § 5 we present the main results of our work. We present

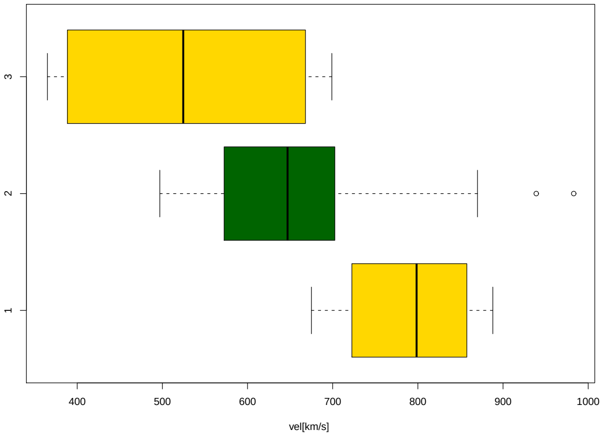

Fig. 1. Statistical significance of the shifting of the X-ray lines found in the spectrum of NGC 3783. Each box is made of five-number summaries: the smallest observation (sample minimum, which are the thin bars at the extreme left of each box), a lower quartile (Q1, which is the left thick border of each box), the median (Q2, black thick vertical line), the upper quartile (Q3, the right thick border of each box) and largest observation (sample maximun, which are the thin bars at the extreme right of each box).

the final physical solution in § 6. We summarize in § 7.

2. SIGNIFICANCE OF THE SHIFTING IN THE X-RAY LINES

Since our analysis searches for possible correlation between the ionization state of the ions forming the absorption lines observed in the X-ray spectrum of this object, and the Doppler velocity shift of those lines, we first study the statistical significance of this possible shifting. A convenient way to do this is through the separation of the ions into groups to search for the velocity shifting. We take all the ions we find in Table 3 (see Table 3 below). The line's centroids are taken from Kaspi et al. (2002). The ionization fraction curves for the classification are taken from Kallman & Bautista (2001); Bautista & Kallman (2001). Afterwards we collect them into three groups[1]: Group 1, representative of all ions of low ionization with ionization parameter $0 < \xi(\mathrm{erg\ cm\ s^{-1}}) < 10$; Group 2, $10 < \xi(\mathrm{erg\ cm\ s^{-1}}) < 250$, representative of intermediate ionization state; and Group 3, $250 < \xi(\mathrm{erg\ cm\ s^{-1}}) < 650$. A graphical way to represent this grouping scheme is shown in Figure 1. Each box is made of five-number summaries: the smallest observation (sample minimum, which is the thin bar at the extreme left of each box); a lower quartile (Q1), which is the left thick border of each box; the median (Q2), the black thick vertical line; upper quartile (Q3), the right thick border of each box and largest observation (sample maximum) which is the thin bar at the extreme right of each box. The first conclusion is that all three Q2s are different. It is clear that Groups 1 and 3 are different at $\gtrsim 1\sigma$. There is overlap between Groups 1 and 2 (possibly due to limited resolution of the instrument), but Groups 2 and 3 are different at $\gtrsim 1\sigma$. We continue our analysis bearing in mind these overlaps in the groups.

[1]We group and generate the figure using the statistical package R (`http://www.r-project.org`).

3. METHOD

Let us consider a radiation source with $L \sim 10^{44} - 10^{47}$ erg s^{-1}, arising from a supermassive ($\sim 10^8\ M_\odot$) black hole (BH). Material $\sim$0.1–1 pc from the BH only needs to absorb a small fraction of this energy to be accelerated to few thousand km s^{-1} in Seyfert galaxies and up to 0.1–0.2 c in high redshift Quasars (Arav, Li, & Begelman 1994; Ramírez 2008; Saez, Chartas, & Brandt 2009; Chartas et al. 2009). By conservation of mass the number density of hydrogen can be written, assuming spherical symmetry, as

$$n_H(r) = \frac{\dot{M}}{4\pi r^2 v(r) \mu m_H}, \qquad (1)$$

where $\dot{M}$ is the mass-loss rate, $v(r)$ is the outflow speed at radius r, μ is the mean atomic weight per hydrogen atom and m_H is the hydrogen mass.

We adopted a velocity law $v(r)$ compatible with the predictions of the radiatively driven wind theory (Castor et al. 1975). The velocity law has two fundamental roles. The first is to shift the frequency of the absorbing lines according to the Doppler effect. The second is to dilute the gas density, affecting radiative transfer across the gas and consequently the ionization and thermal state of the gas. The velocity law varies with distance as

$$w(x) = w_0 + (1 - w_0)\left(1 - \frac{1}{x}\right)^{\beta}. \qquad (2)$$

Here, w is the velocity normalized to the terminal velocity of the wind v_∞, w_0 is the velocity in the base of the wind and x is the distance normalized to the radius of the central core r/r_0. The parameter β is the quantity governing the slope of the velocity with the distance and its *ad hoc* value depends on the type of radiative force acting on the wind. Analysis of hot stars suggests that $0.5 \lesssim \beta \lesssim 1$ (Lamers et al. 1987). The evaluation of radiation-driven wind in AGNs of Drew & Giddings (1982), and more recent dynamical calculations (e.g., Murray et al. 1995; Proga, Stone, & Kallman 2000), suggest that in AGNs $0.5 \lesssim \beta \lesssim 2$. We have computed models using velocity laws $\beta = 0.5, 1, 1.5$ and 2, representing a range from fast ($\beta = 0.5$) to slow winds ($\beta = 2$). We found that fast winds were not able to simultaneously cover the range in velocity and ionization state observed in the spectrum of NGC 3783, needed for the goal of this work, and that the best-fit velocity law was $\beta = 2$. This is why for the rest of this work we use $\beta = 2$. Then, we rewrite the number density in terms of the velocity law as,

$$n_H(x) = n_0 x^{-2} w^{-1}, \tag{3}$$

where $n_0 = \left(\frac{\dot{M}}{4\pi\mu m_H} r_0^{-2} v_\infty^{-1}\right)$. The absorbing line frequencies are shifted according to the Doppler relation,

$$w = \frac{c}{v_\infty}\left(1 - \frac{\lambda}{\lambda_0}\right), \tag{4}$$

where λ_0 is rest wavelength.

Our models are based on clouds illuminated by a point-like X-ray source. The input parameters are the source spectrum, the gas composition, the gas density $n_H(x)$, and the outflow velocity $w(x)$, where x is the position of each slab inside the cloud normalized to the radius of the most exposed face to the source, r_0. The source spectrum is described by the spectral luminosity $L_\epsilon = L f_\epsilon$, where L is the integrated luminosity from 1 to 1000 Ryd, and $\int_1^{1000\mathrm{Ryd}} f_\epsilon d\epsilon = 1$. This spectral function is taken to be a power law $f_\epsilon \sim \epsilon^{-\alpha}$, with $\alpha = 1$. The gas consists of the following elements, H, He, C, N, O, Ne, Mg, Si, S, Ar, Ca and Fe. We use solar abundances of Grevesse, Noels, & Sauval (1996), in all our models.

Thermal and statistical equilibrium in our models are computed with the code XSTAR (Kallman & Bautista 2001; Bautista & Kallman 2001). The code includes all relevant atomic processes and computes the equilibrium temperature and optical depths of the most prominent X-ray and UV lines identified in AGN spectra.

We consider two types of models, the single absorber model (SA) and the multicomponent model (MC). In both cases the absorption line profiles depend simultaneously upon the ionization and the kinematics of the absorbing gas.

3.1. *The Single absorber Model*

This model consists of a single extended cloud directly in the line of sight between the observer and the central source. Such a cloud flows away from the central source and towards the observed. For this model we make use of the Sobolev approximation for computing the line optical depths (Castor et al. 1975),

$$\tau_\nu(r) = \frac{\pi e^2}{mc} f \lambda_0 n_i(r) \left(\frac{dv}{dr}\right)^{-1}, \tag{5}$$

where f is the absorption oscillator strength, λ_0 (in cm) is the laboratory wavelength of the transition, n_i (in cm^{-3}) is the number density of the absorbing ion, and dv/dr is the velocity gradient in the wind. This gives us the relation between the outflow state and the radiation field. This is different from the calculation of the optical depth in the static case, which is directly proportional to the column density.

Inside the cloud we use a one-step forward differencing formula for the radiation transfer (Kallman & McCray 1982)

$$L_\nu(r + \Delta r) = L_\nu(r) e^{-\tau_\nu(r)} + 4\pi r^2 j_\nu(r) \frac{1 - e^{-\tau_\nu(r)}}{\kappa_\nu(r)}, \tag{6}$$

where $j_\nu(r)$ is the emission coefficient at radius r.

Under ionization equilibrium conditions the state of the gas depends just upon the shape of the ionizing spectrum and the ionization parameter ξ, that we define as in Tarter, Tucker, & Salpeter (1969)

$$\xi(r) = \frac{4\pi F(r)}{n_H(r)}, \tag{7}$$

where $F(r)$ is the total ionizing flux,

$$F(r) = \frac{1}{4\pi r^2} \int_1^{1000\mathrm{Ryd}} L_\nu(r) d\nu, \tag{8}$$

with $L_\nu(r)$ given by equation (6). The requirement that ξ spans various orders of magnitude, as observed, yields a cloud geometrically thick throughout most of the spectrum, i.e. a *photoionization bounded* cloud. For instance, a luminosity $L \sim 10^{44}$ erg s^{-1} and $\Delta\xi = \xi_2 - \xi_1 = \frac{L}{n}(\frac{1}{r_2^2} - \frac{1}{r_1^2}) = 10^3$ yield $n \sim 10^6$ cm^{-3} and the column density of the absorbing material is $N_H \sim n\Delta R \sim 9.7 \times 10^{24}$ cm^{-2}. This is a large value, such that even lines with moderately small oscillator strengths become saturated in the emergent spectrum, unless the metal abundances are reduced by several orders of magnitude with respect to solar.

In Figure 2 we compare the computed optical depth for the Ne X λ12.134 line in a stationary nebula with $L = 10^{44}$ erg s^{-1}, and constant density $n = 10^6$ cm^{-3} with a flow with $n(x) = 3.3 \times 10^6 x^{-0.5} w^{-1}$, a wind velocity function with β= 2, and v_∞ =

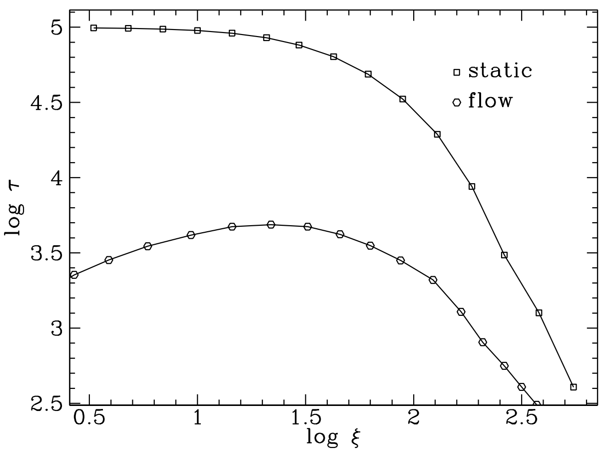

Fig. 2. Optical depth (τ) static case vs outflow model for the line Ne X λ12.134 (see text).

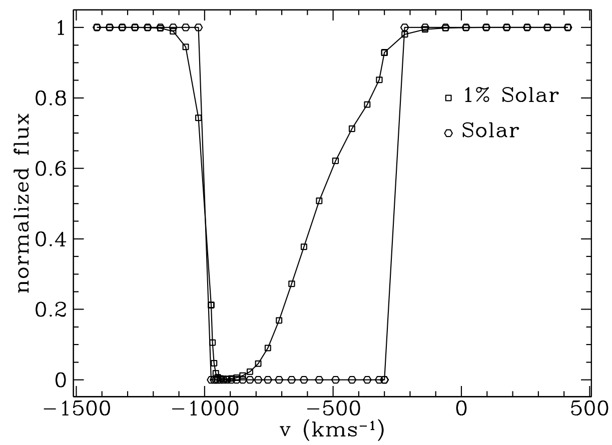

Fig. 3. Profile of the line Ne X λ12.134 formed by taking $F_\lambda(v) = F_c \times \exp[-\tau_\lambda(v)]$ as function of the velocity. The rectangle profile is made by a cloud with solar abundances (open circles). The profile with an extended red wing and a sharp blue wing is made by a cloud with 1% solar abundances (open square).

1000 km s^{-1}. In both cases we adopt a turbulence velocity of 200 km s^{-1} and solar abundances. In the stationary case, τ is proportional the column density of the absorbing material and can reach very large values. In the outflow model, τ peaks at $\log \xi \sim 1.3$ ($v \sim 890$ km s^{-1}) reaching $\sim$5000, that is, nearly two orders of magnitude smaller than in the stationary cloud for the same ξ. Such high optical depths are common to other lines in the X-ray band, like O VIII in the 14–20 Å and the line O VIII λ18.969. In such cases lines appear saturated in the absorption spectrum in contrast with observation. In Ramírez et al. (2005) we fitted the integrated optical depths of resonant lines in the spectrum of NGC 3783 and found $T_{\rm tot} \lesssim 1$ for most of the lines. We illustrate in Figure 3 the consequences of taking this model for the reproduction of the profile of the line Ne X λ12.134. In order to have a non-saturated line (as observed), we had to reduce the abundance to $\sim$1% solar, which has no physical motivation. We do not go further with this model, and present the clumpy (multicomponent) scenario in the next section.

3.2. *The Multicomponent Model*

Now, we examine the scenario in which the absorption profile seen in the X-ray and UV spectra of AGNs are made up of multiple components. The main difference between this model calculations and previous ones by other authors (e.g., Kaspi et al. 2002; Krongold et al. 2003; Różańska et al. 2006), is that in our model all the components are linked by a velocity law and a gas density distribution.

Each absorber is specified by an ionization parameter ξ, a column density N_H, an absorption covering factor, a gas density $n_H(r)$ and an outflow velocity $v(r)$ in order to shift the absorption lines according to the Doppler effect. Once the ionic fraction is calculated from the ionization equations, and the ionic levels computed, the opacity in each frequency bin is

$$\kappa_\nu \rho = \frac{\pi e^2}{m_e c} f_l n_l \left[1 - \frac{n_u g_l}{n_l g_u}\right] \phi(\Delta\nu), \qquad (9)$$

where κ_ν is the opacity at the frequency ν, $\rho = \mu m_H n_H$ is the mass density, f_l is the absorption oscillator strength, n_l, n_u (in cm^{-3}), g_l, g_u are the number density and the statistical weight of the lower and upper levels of the transition, respectively. We allow for the lines to have a finite width characterized by the line profile $\phi(\Delta\nu)$, with a width which is the greater one between the thermal and the turbulent motions. In all our models the turbulence velocity is assumed to be 200 km s^{-1}. The optical depth of a line in each component is

$$\tau_\nu = \int_{r_1}^{r_2} \kappa_\nu(r)\rho(r) dr, \qquad (10)$$

where r_2 and r_1 are the limits of the cloud.

It is important to highlight a special difference between the way we use the ionization parameter in the MC model and the way it is used in the SA model. Because the clouds intervening in this model are optically thin, the ionization parameter at the most exposed face of the cloud remains essentially constant through the cloud, i.e.

$$\xi(r) = \frac{4\pi F(r)}{n_H(r)}, \qquad (11)$$

where $F(r)$ is the total ionizing flux at the radius r.

When two or more outflows are put together they are assumed to be distributed such that the observed spectrum is the result of the addition of all components. Thus, the radiative flux in each bin of frequency for the composite spectrum is

$$F_\nu = \sum_{i=1}^{m} f_\nu(x_i), \tag{12}$$

where m is the number of absorbing clouds in the line-of-sight, $f_\nu(x_i)$ is the flux resulting from the pass of the continuum radiation through the absorbing cloud i, and x_i is the normalized spatial radius of the cloud.

In Ramírez et al. (2005), it is shown that in order to fit the line profiles in NGC 3783 a geometry for the gas distribution different from spherical is required. Such a deviation from spherical geometry has two effects. In the normalized notation the number density is

$$n_H(x) = n_0 x^{-2+\kappa} w^{-1}, \tag{13}$$

where $0 \leq \kappa \leq 2$. A positive value of κ implies that the gas flow dilutes more slowly than in a free spherical expansion, i.e. that there are sources of gas embedded in the flow, or that the flow is confined. A negative value corresponds to sinks of gas in the flow, or expansion of an initially confined flow in a flaring geometry.

Secondly, we allow the radiation flux to have a form

$$F = F_0 \times x^{-2-p}, \tag{14}$$

where p is an index to mimic a deviation of flux from the pure geometrical dilution case. This is expected if the medium between clouds has a significant optical depth (if p is positive) or if there are sources of radiation embedded in the flow (if p is negative).

4. ASSUMPTION ABOUT THE NUMBER DENSITY

Before going into the presentation of the results we would like to highlight important differences between the underlying physical/geometrical motivation of the present work and previous ones. After reviewing the single (geometrically thick) model and the clumpy (geometrically thin) model, we favored the latter, and require for the production of the line profile found in the spectrum of Seyfert galaxies that $\Delta R/R \ll 1$ (also based on results by Gabel et al. (2005) from UV data).

Based on UV CIII* density constraints (Gabel et al. 2005), the electron density for the absorber could be $n_e \approx 10^4$ cm^{-3}. With this (using equation 11 and $n_H \approx n_e/1.2$), the distance between the absorber and the central source is $R \approx 25$ pc ($\approx 10^{20}$ cm). As in Gabel et al. (2005), the low ionization species (XLI in that paper) seems to share the same kinematics with the UV absorber. Using a typical luminosity L for this object of $\approx 10^{44}$ erg s^{-1}, $n_H \approx 10^4$ cm^{-3}, and an ionization parameter of $\xi \approx 1$, $R \approx 10^{20}$ cm; similar to that computed by Gabel et al. (2005); but if we take $n_H \approx 10^{11}$ cm^{-3}, as is required for $\Delta R \ll R$, then $R \approx 10^{16.5}$ cm. This is not in contradiction with Krongold et al. (2005), where they set limits on the density and location of the absorber; with $n_e > 10^4$ cm^{-3}, and $D < 5.7$ pc. However, is clearly different from the computation made by Netzer et al. (2003), of $n_e < 5 \times 10^4$ cm^{-3} $D > 3.2$ pc for the $\log(U_{\rm ox}) = -2.4$ component, $n_e < 10^5$ cm^{-3} $D > 0.63$ pc for the $\log(U_{\rm ox}) = -1.2$ component, and $n_e < 2.5 \times 10^5$ cm^{-3} $D > 0.18$ pc for the $\log(U_{\rm ox}) = -0.6$ component. It is clear that some of the differences in the estimations can be due to differences in the nature of the physics behind the estimations. In Krongold et al. (2005) (and also Reeves et al. 2004, for the Fe K shell), the fundamental assumption behind the computation of n_e is that the absorber responds instantaneously to changes of flux of the ionizing source, while in Netzer et al. (2003) the estimations are based on temperature derived models, average recombination rates and no response to continuum variations on timescales of 10 days. And, for our purposes, this basically translates into differences between the two proposed physical mechanisms: thermally accelerated winds, which in principle have to consider a sublimination radius for the material not being evaporated, and radiatively accelerated winds with origin possibly in the accretion disk of subparsec scale; both are competitor theories in the explanation of the origen of the warm-absorber outflows.

5. RESULTS AND DISCUSSIONS

In Figure 4 we show the variation of the different variables governing the kinematics and the ionization structure of one of our models (model A). This is a wind with a velocity slope $\beta = 2$, $\kappa = 1.5$ and $p = 1.5$. The number of kinematic components m is 11. The assumed abundance is solar, as is given in Table 1, and each component has a column density $N_H = 5 \times 10^{20}$ cm^{-2}. In this model the variation in the ionization parameter is $\log \xi = 3.5 - (-0.65)$ [erg cm s^{-1}], where the "launching" ionization parameter is defined as $\log \xi_0 = 3.5$ [erg cm s^{-1}], and the variation in density $\log n_H = 11.4 - 10.26$ [cm^{-3}].

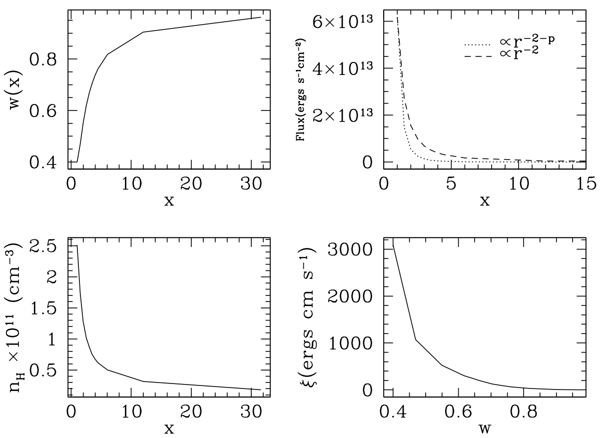

Fig. 4. Variation of the main kinematic and ionization variables for model A (see text). Upper left: Velocity law $w(x)$ for the model. Upper right: The ionizing radiative flux, decaying as $\propto r^{-2}$ (dashed line) and as $\propto r^{-2-p}$ (dotted line). Lower left: Variation of the density as function of x. Lower right: Variation of the ionization parameter (ξ) with the normalized velocity.

TABLE 1

COMPOSITION AND PARAMETER VALUES OF THE KINEMATIC MODEL A[a]

Element	Relative Abundance
H	1.0
He	0.1
C	0.3540E-03
N	0.9330E-04
O	0.7410E-03
Ne	0.1200E-03
Mg	0.3800E-04
Si	0.3550E-04
S	0.2140E-04
Ar	0.3310E-05
Ca	0.2290E-05
Fe	0.3160E-04

[a]In this model $w_0 = 0.4$, $v_\infty = 900$ km s^{-1}, $\log_{10} r_0 = 15.75$ [cm], $v_{\rm turb} = 200$ km s^{-1} and $N_H = 5\times10^{20}$ cm^{-2}.

We can see the variation with distance of the input parameters w, flux, n_H and ξ, for model A in Figure 4. In Figure 5 we plot the velocity shifts taken from the maximum line optical depths $\tau_{\rm max}$ of our model versus the line centroids measured by Kaspi et al. (2002) for NGC 3783 (see Table 3 in that paper).

We fit a linear model by robust regression using the M estimator (Huber 1964). The weights are included as the inverse of the variances, with the variance equal to $\Delta v = (v_{\rm lo} + v_{\rm hi})/2$, and $v_{\rm lo}$, and $v_{\rm hi}$ are the differences between centroid and lower and upper velocity limits of the measured lines given in Table 3 of Kaspi et al. (2002). The best-fit slope is 0.97±0.31 (solid line in the figure), and the residual standard error (rms) is 15.4 for 25 degrees of freedom (dof). The agreement is encouraging, considering that no model has been suggested before to explain the possible correlation between the ionization parameter and the velocity shift seen in this Seyfert galaxy.

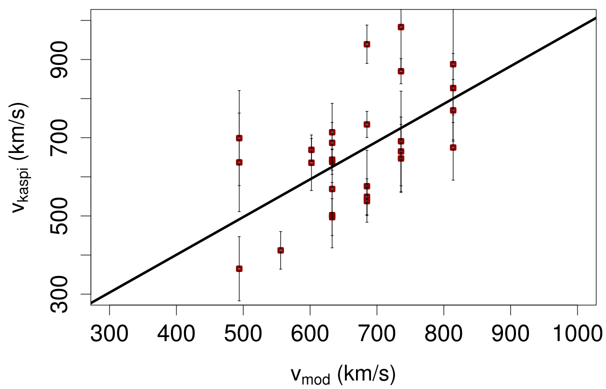

Fig. 5. Measured vs model predicted velocities for the group of unblended lines given in Table 2 of Ramírez et al. (2005). The measurements are taken from Kaspi et al. (2002). The solid line is the best line after a linear regression for model A.

Although the velocity shifts measured with respect to line minima are well explained by this model the distribution (in general) of the line profile shapes is not in agreement with that reported in Ramírez et al. (2005), for instance. From that study, most lines have extended blue wings. On the other hand, the model does predict the correct asymmetries for a few lines from highly ionized species, but the profiles of the lower ionizations lines exhibit more extended red wings, unlike the observations. The discrepancy between the modeled profile of the O VIII λ18.9 line and that observed in NGC 3783 is important. This is why we created model B.

In Figure 6 we present the variation of the variables governing the kinematics and the ionization structure of another model (model B). Here we change slightly the parameters $\log\xi_0$, and v_∞ (see Table 2 for details). The wind has the parameters $\beta = 2$, $\kappa = 1.5$ and $p = 1.5$. The number of kinematic components m is 11. The abundances and the column density are as in model A. In this model the variations in ionization parameter and density are $\log\xi = 3.00 - (-1.13)$ [erg cm s^{-1}] and

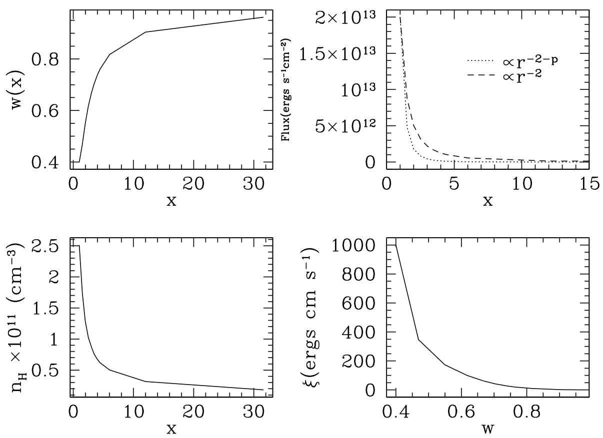

Fig. 6. Variation of the main kinematic and ionization variables for model B (see text). Upper left: Velocity law $w(x)$ for the model. Upper right: The ionizing radiative flux, decaying as $\propto r^{-2}$ (dashed line) and as $\propto r^{-2-p}$ (dotted line). Lower left: Variation of the density as function of x. Lower right: Variation of the ionization parameter (ξ) with the normalized velocity.

TABLE 2

COMPOSITION AND PARAMETER VALUES OF THE KINEMATIC MODEL B[a]

Element	Relative Abundance
H	1.0
He	0.1
C	0.3540E-03
N	0.9330E-04
O	0.7410E-03
Ne	0.1200E-03
Mg	0.3800E-04
Si	0.3550E-04
S	0.2140E-04
Ar	0.3310E-05
Ca	0.2290E-05
Fe	0.3160E-04

[a]In this model $w_0 = 0.4$, $v_\infty = 1100$ km s^{-1}, $\log_{10} r_0 = 15.75$ [cm], $v_{\rm turb} = 200$ km s^{-1} and $N_H = 5 \times 10^{20}$ cm^{-2}.

$\log n_H = 11.40 - 10.26$ [cm^{-3}]. We compare models A and B in terms of the variation of optical depth vs. velocity of the flows of three important lines, i.e, Si XIV λ6.182, Si XIII λ6.648 and Mg XII λ7.106. We could estimate the contribution of each cloud to the formation of the composite profiles of these lines. We note that model B is superior to model A in describing the low-velocity portion of the flow reflected by the high ionization lines seen in NGC 3783 (extended blue wings), but yields a worse description of the spectrum at the higher terminal velocities responsible for the center of the lines measured by Kaspi et al. (2002).

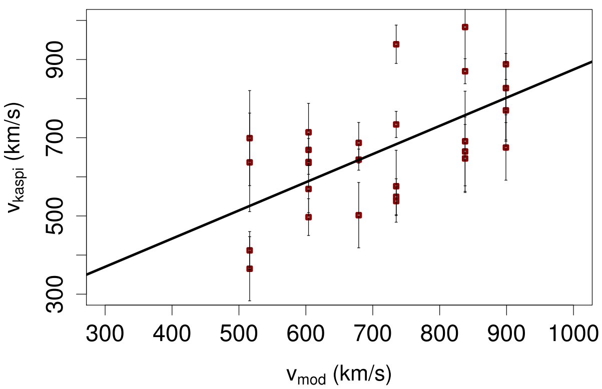

Fig. 7. Measured vs model predicted velocities for the group of unblended lines given in Table 2 of Ramírez et al. (2005). The measurements are taken from Kaspi et al. (2002). The solid line is the best line after a linear regression for model B.

Figure 7 shows the fit of a linear model by robust regression using the M estimator for model B. As in model A, the weights are included as the inverse of the variances, with the variance equal to $\Delta v = (v_{\rm lo} + v_{\rm hi})/2$, and $v_{\rm lo}$, and $v_{\rm hi}$ are the differences between centroid and the lower and upper velocity limits of the measured lines given in Table 3 of Kaspi et al. (2002). The best-fit slope is 0.72 ± 0.20 (solid line in the figure), and the residual standard error (rms) is 17.6 for 25 degrees of freedom (dof). In general, the scatter becomes worse for lines with terminal velocities greater than 1100 km s^{-1}.

5.1. *Modeling global properties - ξ vs velocity*

One of the prime goals of this study is to examine the relationship between the kinematics and the ionization structure of the flow. This is complementary to earlier work (Krongold et al. 2003; Netzer et al. 2003; Krongold et al. 2005) which follows the algorithm of constructing a grid of static photoionization models, with varying ionization parameter and column density, with the selection of this quantities which best reproduce the EW observed in the spectra, in addition to paying attention to the relationship between these physical parameters and the position in wavelength space of the absorption troughs.

Krongold et al. (2003) fitted photoionization models to the 900 ks spectrum of NGC 3783 using

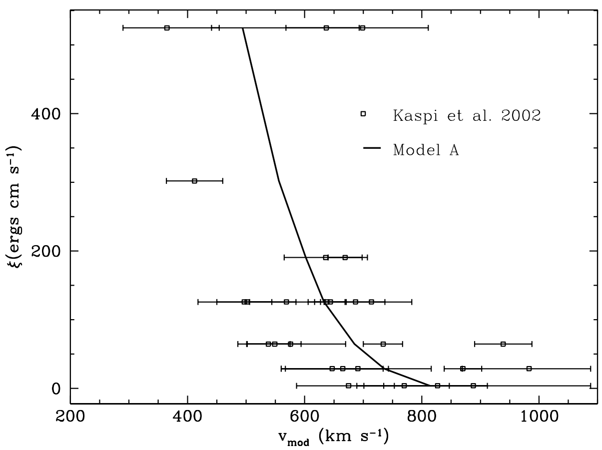

Fig. 8. Relationship between the ionization parameter and velocity. The solid line is the theoretical prediction for model A. The open squares with error bars are points with velocities taken from Kaspi et al. (2002), for the group of lines compared in Figure 5.

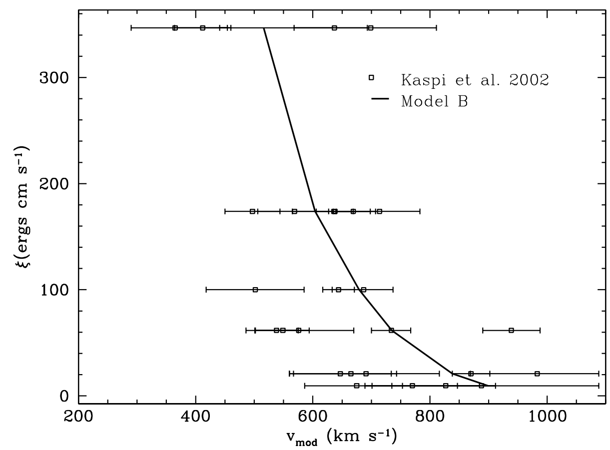

Fig. 9. Relationship between the ionization parameter and velocity. The solid line is the theoretical prediction for model B. The open squares with error bars are points with velocities taken from Kaspi et al. (2002), for the group of lines compared in Figure 7.

two phases; one at high ionization and high temperature log $T \sim 5.98$ (HIP) and one at low ionization and temperature log $T \sim 4.41$ (LIP), finding good agreement between the modeled equivalent width (EW) and the measured one for a set of absorption lines (see Figure 9 of Krongold et al. 2003). They set each of these phases at a single outflow velocity of $\sim$750 km s^{-1}, assuming spatial coexistence of the two absorbers. The approach was similar to that from Netzer et al. (2003), but in the latter they used three components in pressure equilibrium, with two kinematic components each.

One property of our model is the capability of allowing the possibility of establishing[2] a relationship between the ionization and the kinematics of the gas based on a radiatively accelerated wind. Figures 8 and 9 show this relation for models A and B, respectively. These plots show the predicted relationship between the observed velocities and the ionization parameter. While absorption from highly ionized ions originates from low-to-intermediate (200–600 km s^{-1}) velocities, lines from lower ionization stages are formed at intermediate-to-high velocities (600–1000 km s^{-1}).

5.2. *Far-UV and UV absorbers*

The relationship between the X-ray absorption spectrum and the UV absorption spectrum is at present a subject of controversy. Kraemer, Crenshaw, & Gabel (2001) and Gabel et al.

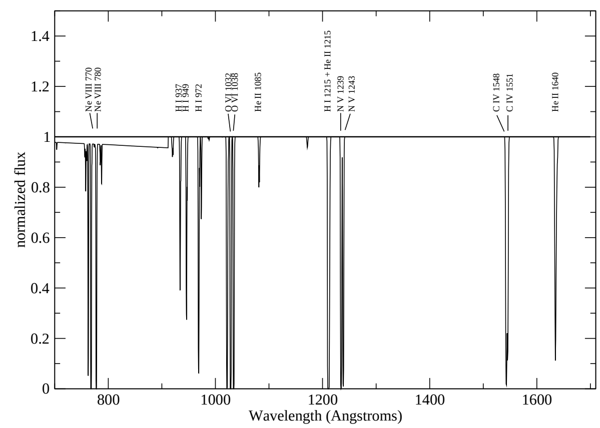

Fig. 10. Predicted UV spectrum by model B (in the range 700–1700 Å). These absorption lines are formed by the faster (or at lower ionization parameters) clouds of model B, i.e., $\log\xi = 0.12, -0.65$. Most of these lines are found in real UV spectra of AGN.

(2003, 2005) have analyzed de UV spectrum of NGC 3783. HST/STIS and FUSE spectra show absorption troughs from the low order Lyman series (i.e. Lyα, Lyβ, Lyγ), C IV $\lambda\lambda1548.2, 1550.8$, N V $\lambda\lambda1238.8, 1242.8$, O VI $\lambda\lambda1032, 1038$. All these lines are seen in three kinematic components at -1365, -548, and -724 km s^{-1} (components 1, 2 and 3 respectively). A weak fourth component is reported by Gabel et al. (2003, 2005) at -1027 km s^{-1}. Figure 10 shows the spectrum predicted by model B in the range 700–1700 Å. It is clear from this figure that lines due to the low order Lyman series, He II, C IV, N V, O VI, and Ne VIII would be

[2] We explicitly state *allow the possibility*, since the limited resolution of the telescope does not allow us to go beyond this possibility.

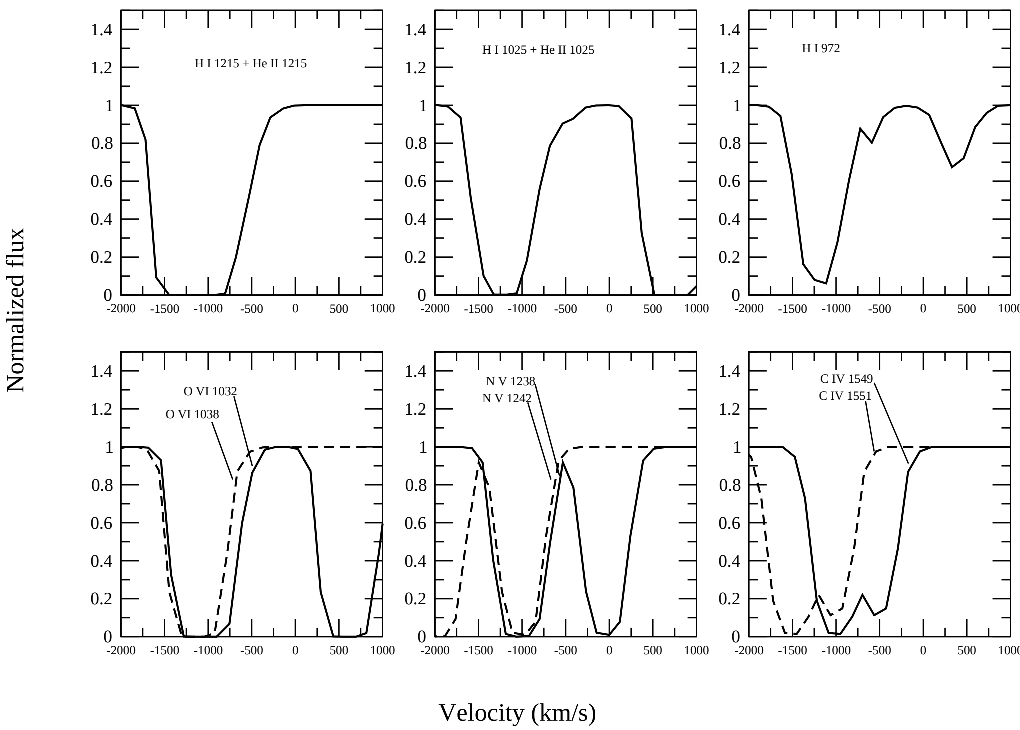

Fig. 11. Predicted UV spectrum by model B (in velocity space). These absorption lines are formed by the faster clouds (or by those at lower ionization parameters) of model B, i.e., $\log \xi = 0.12, -0.65$. Some of the velocities displayed by these lines are shared by lines coming from the X-ray band. For transforming to velocity space, we have taken the shorter rest-wavelength of the doublet (solid line), and also the longer rest-wavelength of the doublet (dashed line).

detectable in the UV band of the spectrum. Figure 11 shows the spectra of several UV lines as a function of radial velocity with respect to the systemic one. At the top of the figure we present the Lyα blended with the He II $\lambda 1215$ line (upper left) which yields a feature centered at ~ -1300 km s^{-1}. Also, an absorption feature is formed with the Lyβ and He II $\lambda 1025$ lines (upper center) with center at ~ -1200 km s^{-1}, and the line Lyγ (upper right) with a velocity ~ -1100 km s^{-1}. At the bottom of the figure we plot the spectrum of three important doublets (C IV $\lambda\lambda 1548.2, 1550.8$, N V $\lambda\lambda 1238.8, 1242.8$, and O VI $\lambda\lambda 1032, 1038$). The solid line depicts the velocity spectra constructed taking the shorter wavelength of the doublet. The spectra shown as dashed lines were obtained taking the longer wavelength. One can see the similarity between the velocities predicted by our model and the high-velocity components (1, 4 and likely 3) seen in the UV spectrum of NGC 3783 and other Seyfert 1 galaxies (for example NGC 5548). This is similar to the conclusion reached by Gabel et al. (2005), based on Kaspi et al. (2002) and Gabel et al. (2003), where all X-ray lines having sufficiently high resolution and S/N were found to span the radial velocities of the three UV kinematic components (see also next section). These are predictions which arise naturally from our model because we are modeling the wind self-consistently with a complete treatment of radiative processes in all wavelengths. In our models these UV features as well as the long wavelength absorption lines in the X-ray band, are produced by the low ionization parameter part of the flow (e.g., $\log \xi = 0.12, -1.13$ from Figure 6 lower right panel). This demonstrates that the same absorber can produce X-ray and UV lines with similar velocities. Figure 12 shows the kinematic relationship between the X-ray and the UV absorbers. The model has been shifted (up) for clarity. Here we show the O VIII $\lambda 18.969$ and the doublet O VI $\lambda\lambda 1032, 1038$ (with respect to the shorter wavelength). For comparison we plot the histogram data of the 900 ks of NGC 3783. We see that our model is capable of simultaneously producing X-ray and UV absorption lines with similar velocities around ~ 1000 km s^{-1}, as it has been suggested from UV data (Gabel et al. 2003).

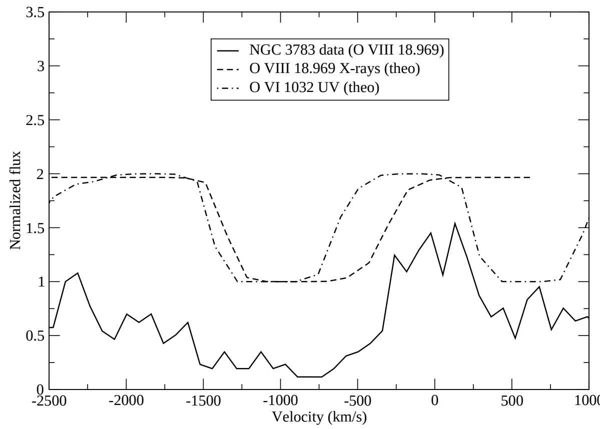

Fig. 12. Possible kinematical relationship between the UV and the X-ray absorbers. In the figure are plotted the theoretical X-ray and UV lines O VIII λ18.969 and O VI λ1032, dashed and short-dotted lines respectively. Also plotted is the profile of the line O VIII λ18.969 taken from the 900 ks spectrum of NGC 3783. All these lines are sharing velocities $\sim$1000 km s^{-1}.

5.3. *Present single wind vs multiphase wind scenario*

However, we want to highlight the most important differences between our model, consisting of a single wind governed by the laws of radiative acceleration, and the multiphase wind subjected to pressure equilibrium.

The first difference is that in our model there is a clear correlation between ionization state of the ions and velocity ($\xi - v$), and ξ and number of particle n_H ($\xi - n_H$). At the same time, because of the dependence of v and n_H on the spatial distance r, there is a dependence of ξ on r. This is different from the multicomponent in pressure equilibrium model, suggested by Netzer et al. (2003). In that model three components (in ionization) may coexist in the same volume of space and lie on the stable regions of the nearly vertical part of the thermal stability curve (log T *vs* log $[U/T]$, see Figure 12 in that paper). Our absorbers are not embedded in an external medium, and they cannot coexist at exactly the same location, but rather follow the physical laws of radiative acceleration. In this context, Gabel et al. (2005) also find that the UV absorbers of NGC 3783 may share some properties of the multiphase thermal wind. The UV kinematic components 1b, 2 and 3 could occupy the low-temperature base of the region of the thermal stability curve where a range of temperatures can coexist in pressure equilibrium. There is one weak point in the picture of inhomogeneities coexisting in pressure equilibrium. The low-ionization high-velocity UV absorber does not fit there, due to a pressure of a factor of 10 larger than that of the other component. If embedded into a more ionized-hotter material, it will eventually evaporate, unless there exists an additional confining mechanism. This extra confinement could be provided by magnetic pressure, requiring moderate magnetic fields ($B \approx 10^{-3}$ G), as predicted by some dynamical models (Emmering, Blandford, & Shlosman 1992; de Kool & Begelman 1995). In our model, there is no need for a confining mechanism, and if anything, the more ionized material is closer to the source, shielding the intense continuum radiation and preventing its evaporation. We conclude by stating that our model represents an additional competitor. It cannot be ruled out by comparison with the pressure equilibrium model. A more detailed comparison between models is beyond the scope of the present work, but could take place in the future.

6. TWO OUTFLOWS

So far we have been concerned with the line velocity shifts as measured with respect to the points of maximum absorption of the lines, but little has been said about the asymmetry of the troughs. To quantify the line asymmetries predicted by the theoretical models we have tabulated the fraction of the terminal velocity at which the absorption is maximum, to be compared with the ratio ($\bar{v}/v_1$), where v_1 is the position of the blue edge of each line, used to quantify the asymmetry in the spectrum of NGC 3783 (see Table 3 Ramírez et al. 2005). We characterize a theoretical line as "red" if $v(\tau_{\max})/v_\infty > 0.5$ and as "blue" if $v(\tau_{\max})/v_\infty < 0.5$, while for observed lines they are grouped according to $\bar{v}/v_1 > 0.5$ and $\bar{v}/v_1 < 0.5$ (see Ramírez et al. 2005). In Table 3 we present the observed troughs. In the first and second columns are given the identifications and the wavelengths of the lines, in the third, the fraction $v(\tau_{\max})/v_\infty$ for model A, and in the fourth the classification from observed lines, as in Ramírez et al. (2005), i.e., $\bar{v}/v_1$. We classify every trough as either (R) if it is red or (B) if it is blue. There are clear discrepancies between model A and the observations. In order to improve the agreement with observations we found it necessary to create a model composed of two outflows, which differ by their log ξ_0, the initial exposition to the source. In Table 4 we can see separately the parameters of the two outflows which compose model C. The first flow, with $\log \xi_0 = 3$, which we call HIF (high ionization flow), is able to create the majority of the high ionization lines (S XVI λ4.729, S XV λ5.039, Fe XXIII λ8.303), with

TABLE 3

ASYMMETRY COMPARISON BETWEEN MODEL A AND OBSERVATIONS

Ion	Line (Å)	$v(\tau_{\max})/900$ km s^{-1}	Ramírez et al. (2005)[a]
S XVI	4.729	0.55 (R)	0.33±0.1 (B)
S XV	5.039	0.67 (R)	0.23±0.1 (B)
Si XIII	5.681	0.70 (R)	0.35±0.1 (B)
Si XIV	6.182	0.67 (R)	0.23±0.08 (B)
Si XIII	6.648	0.70 (R)	0.43±0.074 (B)
Mg XII	7.106	0.70 (R)	0.32±0.070 (B)
Mg XI	7.473	0.76 (R)	0.74±0.067 (R)
Fe XXIII	8.303	0.55 (R)	0.037±0.060 (B)
Mg XII	8.421	0.70 (R)	0.32±0.059 (B)
Mg XI	9.169	0.76 (R)	0.31±0.054 (B)
Ne X	9.708	0.76 (R)	0.45±0.052 (B)
Ne X	10.240	0.76 (R)	0.17±0.048 (B)
Ne IX	11.547	0.82 (R)	0.69±0.043 (R)
Fe XXII	11.770	0.55 (R)	0.22±0.042 (B)
Ne X	12.134	0.76 (R)	0.29±0.041 (B)
Fe XXI	12.284	0.62 (R)	0.42±0.040 (B)
Fe XVIII	14.373	0.70 (R)	0.27±0.035 (B)
Fe XVIII	14.534	0.70 (R)	0.51±0.034 (R)
O VIII	14.832	0.82 (R)	0.21±0.033 (B)
Fe XVII	15.015	0.70 (R)	0.76±0.033 (R)
O VIII	15.188	0.82 (R)	0.38±0.033 (B)
O VIII	16.006	0.82 (R)	0.26±0.030 (B)
O VII	17.200	0.90 (R)	0.29±0.029 (B)
O VII	17.396	0.90 (R)	0.30±0.029 (B)
O VII	17.768	0.90 (R)	0.32±0.028 (B)
O VII	18.627	0.90 (R)	0.32±0.027 (B)
O VIII	18.969	0.82 (R)	0.26±0.026 (B)

[a]$\bar{v}/v_1$, see definition in the text.

extended blue wings, as the flow moves outwards and acquires more velocity, in agreement with the observations. The second, which we call LIF (low ionization flow), characterized by $\log \xi_0 = 2$, is able to create the extended blue wing of the oxygen lines. This model has the fundamental ingredients that explain the asymmetry observed in the lines of NGC 3783 and, at the same time, gives us the bulk velocity of the flow.

In the third column of Table 5 we present the characterization of the lines coming from the two-outflow model. The HIF component is the major contributor to the formation of the high ionization lines, i.e. S XVI, Fe XXI, Fe XXII, Fe XXIII, because their optical depths peak close to $\log \xi_0$ (HIF), and as the velocity of the flow increases their ionization fraction decreases, forming their blue wings. Under this picture, only a few lines are characterized as blue, while the rest are red. Some intermediate-to-low-ionization ions have appreciable fractions in the LIF component, which broadens the lines and yields

TABLE 4

PARAMETERS OF THE TWO OUTFLOW MODEL (MODEL C)

Outflow HIF	Outflow LIF
$\log \xi_0 = 3.0$	$\log \xi_0 = 2.0$
$v_\infty = 1100$ km s^{-1}	$v_\infty = 2200$ km s^{-1}
$N_H = 10^{22}$ cm^{-2}	$N_H = 10^{21}$ cm^{-2}
$w_0 = 0.4$	$w_0 = 0.2$
Solar composition	Solar composition

TABLE 5

ASYMMETRY COMPARISON BETWEEN MODEL C AND OBSERVATIONS

Ion	Line (Å)	$v(\tau_{\max}[\text{HIF}])/1100$ km s^{-1}	$v(\tau_{\max}[\text{HIF+LIF}])/2200$ km s^{-1}
S XVI	4.729	0.47 (B)	0.47 (B)
S XV	5.039	0.55 (R)	0.55 (R)
Si XIII	5.681	0.62 (R)	0.62 (R)
Si XIV	6.182	0.55 (R)	0.55 (R)
Si XIII	6.648	0.62 (R)	0.62 (R)
Mg XII	7.106	0.55 (R)	0.55 (R)
Mg XI	7.473	0.74 (R)	0.74 (R)
Fe XXIII	8.303	0.47 (B)	0.47 (B)
Mg XII	8.421	0.55 (R)	0.55 (R)
Mg XI	9.169	0.74 (R)	0.37 (B)[a]
Ne X	9.708	0.74 (R)	0.74 (R)
Ne X	10.240	0.74 (R)	0.37 (B)[a]
Ne IX	11.547	0.74 (R)	0.37 (B)[a]
Fe XXII	11.770	0.47 (B)	0.47 (B)
Ne X	12.134	0.74 (R)	0.37 (B)[a]
Fe XXI	12.284	0.47 (B)	0.47 (B)
Fe XVIII	14.373	0.55 (R)	0.55 (R)
Fe XVIII	14.534	0.55 (R)	0.55 (R)
O VIII	14.832	0.74 (R)	0.37 (B)[a]
Fe XVII	15.015	0.62 (R)	0.62 (R)
O VIII	15.188	0.74 (R)	0.37 (B)[a]
O VIII	16.006	0.74 (R)	0.37 (B)[a]
O VII	17.200	0.82 (R)	0.41 (B)[a]
O VII	17.396	0.82 (R)	0.41 (B)[a]
O VII	17.768	0.82 (R)	0.41 (B)[a]
O VII	18.627	0.82 (R)	0.41 (B)[a]
O VIII	18.969	0.74 (R)	0.37 (B)[a]

[a]With the addition of the LIF, we mark those line whose symmetry change.

a red appearance to the composed profile. This effect is illustrated by the fourth column of Table 5.

The composite model reproduces the asymmetry of the lines. The present uncertainties in the computation of $v(\tau_{\max})$ are of the order of 60 km s^{-1} (or $\Delta v(\tau_{\max})/v_\infty = 0.055$ with $v_\infty = 1100$ km s^{-1}). So the lines classified as pure red with $v(\tau_{\max})/v_\infty \gtrsim 0.55$ and pure blue with $v(\tau_{\max})/v_\infty \lesssim 0.45$ are more reliable than those with $0.45 \lesssim v(\tau_{\max})/v_\infty \lesssim 0.55$.

It is interesting to analyze why the O VII and O VIII lines are blue, while the lines Mg XI λ7.473 and Fe XVII λ15.015 remain red. The optical depths of Mg XI λ7.473, and Fe XVII λ15.015 are below 10^{-4} at velocities greater than 1100 km s^{-1}, so the LIF component does not contribute to their broadening. Another interesting example is the difference in classification between the lines Mg XI λ7.473 and Mg XI λ9.169. The reason is that while for Mg XI λ7.473 the oscillator strength is $\sim 5 \times 10^{-2}$, the f-value for the line Mg XI λ9.169 is almost one order of magnitude larger ($\sim 7 \times 10^{-1}$), which causes the optical depth of the latter to be significant up to velocities beyond $\sim$1600 km s^{-1}.

Figure 13 compares the modeled velocities of the lines from the two-outflow model with observations. Robust regression using the M estimator gives a slope of 0.63 ± 0.22 (solid line in the figure), and the residual standard error (rms) is 16.6 for 25 degrees of freedom (dof).

A comparison between the predicted trough profiles and those observed in NGC 3783 is shown in Figure 14. Here we plot the theoretical spectrum given by the outflows HIF and LIF in the 18.5–19.3 Å. We have used a power law as continuum, with a spectral

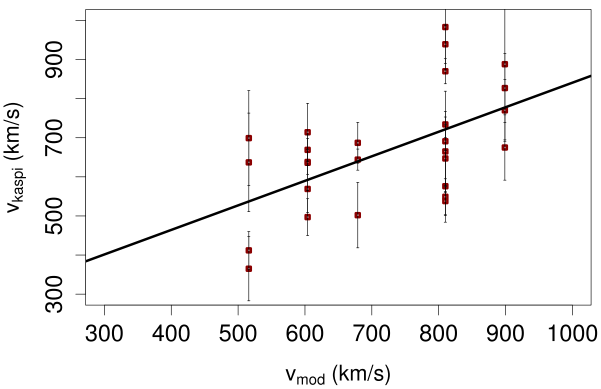

Fig. 13. Measured vs model-predicted velocities for the group of unblended lines given in Table 2 of Ramírez et al. (2005). The measurements are taken from Kaspi et al. (2002). The solid line is the best line after a linear regression for model C.

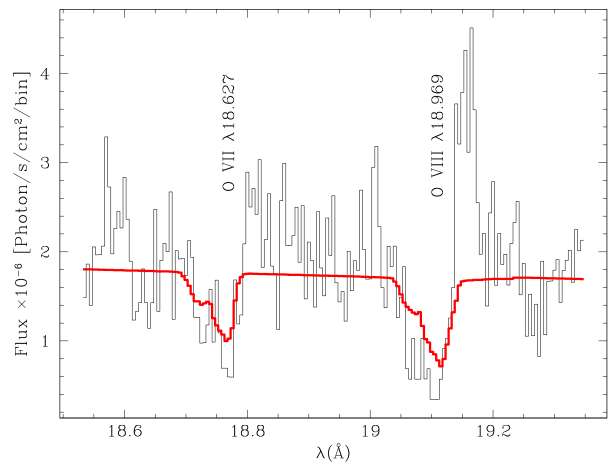

Fig. 14. A graphical representation of the flows HIF and LIF with the line profiles seen in NGC 3783 (histogram). Solid line is the composite model (model C) with two flows. It can be seen that it was necessary to include the second low-ionization flow in order to reproduce the asymmetry of these lines. Otherwise the high-ionization flow would form a more extended red wing.

index of $\Gamma = 1.77$, suitable for this AGN, and have set an extra absorber `the wabs`[3] model in XSPEC, and the composite fluxes generated by the HIF and the LIF components. To compose the O VIII λ18.969 line profile we have summed the fluxes from both flows using equation (12) (where $m = 22$). With this approximation the profile predicted by the two-outflow model is in excellent agreement with observations (Ramírez et al. 2005). The red wing of the troughs in the range 0–1000 km s^{-1} is formed by the HIF, while the blue wing in the range ∼1000–2500 km s^{-1} is formed by the LIF. These values are in agreement with the values measured for this lines in the observed spectrum.

This is the first time that such theoretical work has been carried out to explain the asymmetry seen in absorption in the X-ray spectrum of AGNs. Other work has been able to explain the blue wings of UV lines, like the well-studied C IV λ 1549, for example from radiation-driven disk-wind models (Proga 2003). So we cannot conclude that the model presented here is unique for the description of the asymmetry seen in X-ray lines of AGNs, until detailed comparisons are made with such models, including the X-ray line profile produced by a wind from a Keplerian accretion disk (Knigge, Woods, & Drew 1995; Shlosman, Vitello, & Mauche 1996; Proga et al. 2000; Drew & Proga 2000). Further work is necessary for such a comparison, and we plan to do that in a near future.

7. SUMMARY

We have computed photoionized wind-flow models for the X-ray spectrum of NGC 3783. We studied single continously absorbing models, as well as multiple optically thin components linked through an analytic wind velocity law. We found that the single continuously absorbing model yields gas column densities and optical depths that are too large, unless one adopts very low ($\sim 10^{3-4}$ cm^{-3}) densities and metal abundances (∼0.01 solar). On the other hand, the multicomponent model is able to reproduce observations very well. For this model we compute ionization properties of the material using a velocity law compatible with a radiative wind. Our model is consistent with $\log n_0 \sim 11.35$ [cm^{-3}], a launching radii of $\log r_0 \sim 15$ [cm], and a terminal velocities of $v_\infty \sim 1500$ km s^{-1}, which yield a mass loss rate of the order of $\dot{M}_{\rm out} \sim 1\ M_\odot$/yr (assuming a volumetric factor $f_{\rm vol} = 0.1$). If we assume an ionizing luminosity $L \sim 2 \times 10^{44}$ erg s^{-1} (Peterson et al. 2004), and an accretion efficiency of $\eta = 0.1$, the Eddington mass accretion rate is $\dot{M}_{\rm edd} \sim 0.01\ M_\odot$/yr. This is consistent with the result of Crenshaw & Kraemer (2007) for NGC 4151, and Ramírez (2008) for APM 08279+5255, of $\dot{M}_{\rm out}/\dot{M}_{\rm edd} > 10$. However, it is different from the supposition made by Gonçalves et al. (2006), of $\dot{M}_{\rm out}/\dot{M}_{\rm edd} \leq 1$, using their photoionization code TITAN, for computing the single medium in pressure equilibrium.

Finally, the asymmetry seen in the lines of the X-ray spectrum of NGC 3783 required a model with two outflows. One flow, with a launching ionization parameter of $\log \xi_0 \sim 3$ and a column density of

[3] $N_{\rm wabs} = 0.1 \times 10^{22}$ cm^{-2}.

$N_H = 10^{22}$ cm^{-2}, recreates the red wings of the low ionization lines from Ne IX to O VII, and the blue wings of the high ionization lines from Fe XXIII to Si XIV. A second flow is necessary to create the blue wing of the oxygen lines, which exhibit a blue character. The theoretical fitting required $\log \xi_0 \sim 2$, terminal velocities of around $\sim$2200 km s^{-1}, and a column density of $N_H = 10^{21}$ cm^{-2}.

Our calculations also predict a relationship between the UV and X-ray bands, as models adjusted to fit the X-ray spectrum naturally predict UV lines like the Lyman serie, and the O VI, N V and C IV doublets, in apparent concordance with Costantini (2010).

REFERENCES

Arav, N., Li, Z., & Begelman, M. C. 1994, ApJ, 432, 62
Bautista, M. A., & Kallman, T. R. 2001, ApJS, 134, 139
Castor, J. I., Abbott, D. C., & Klein, R. I. 1975, ApJ, 195, 157
Chartas, G., Saez, C., Brandt, W. N., Giustini, M., & Garmire, G. P. 2009, ApJ, 706, 644
Costantini, E. 2010, Space Science Reviews, 157, 265
Crenshaw, D. M., & Kraemer, S. B. 2007, ApJ, 659, 250
de Kool, M., & Begelman, M. C. 1995, ApJ, 455, 448
Drew, J. E. 1989, ApJS, 71, 267
Drew, J., & Giddings, J. 1982, MNRAS, 201, 27
Drew, J. E., & Proga, D. 2000, NewA Rev., 44, 21
Drew, J., & Verbunt, F. 1985, MNRAS, 213, 191
Elvis, M. 2000, ApJ, 545, 63
Emmering, R. T., Blandford, R. D., & Shlosman, I. 1992, ApJ, 385, 460
Gabel, J. R., et al. 2003, ApJ, 583, 178
Gabel, J. R., et al. 2005, ApJ, 631, 741
George, I. M., Turner, T. J., Netzer, H., Nandra, K., Mushotzky, R. F., & Yaqoob, T. 1998, ApJS, 114, 73
Gonçalves, A. C., Collin, S., Dumont, A., Mouchet, M., Różańska, A., Chevallier, L., & Goosmann, R. W. 2006, A&A, 451, L23
Grevesse, N., Noels, A., & Sauval, A. J. 1996, in ASP Conf. Ser. 99, Cosmic Abundances, ed. S. Holt & G. Sonneborn (San Francisco: ASP), 117
Huber, P. J. 1964, Ann. Math. Statist., 35, 73
Kaastra, J. S., Mewe, R., Liedahl, D. A., Komossa, S., & Brinkman, A. C. 2000, A&A, 354, L83
Kallman, T., & Bautista, M. 2001, ApJS, 133, 221
Kallman, T. R., & McCray, R. 1982, ApJS, 50, 263
Kaspi, S., Brandt, W. N., Netzer, H., Sambruna, R., Chartas, G., Garmire, G. P., & Nousek, J. A. 2000, ApJ, 535, L17
Kaspi, S., et al. 2002, ApJ, 574, 643
Kaspi, S., et al. 2001, ApJ, 554, 216
Knigge, C., Woods, J. A., & Drew, J. E. 1995, MNRAS, 273, 225
Komossa, S. 1999, in ASCA/ROSAT Workshop on AGN and the X-Ray Background, ed. T. Takahashi & H. Inoue (ISAS Rep. 149) (Tokyo: ISAS), 149
Kraemer, S. B., Crenshaw, D. M., & Gabel, J. R. 2001, ApJ, 557, 30
Krolik, J. H., & Kriss, G. A. 2001, ApJ, 561, 684
Krongold, Y., Nicastro, F., Brickhouse, N. S., Elvis, M., Liedahl, D. A., & Mathur, S. 2003, ApJ, 597, 832
Krongold, Y., Nicastro, F., Elvis, M., Brickhouse, N. S., Mathur, S., & Zezas, A. 2005, ApJ, 620, 165
Lamers, H. J. G. L. M., Cerruti-Sola, M., & Perinotto, M. 1987, ApJ, 314, 726
Murray, N., Chiang, J., Grossman, S. A., & Voit, G. M. 1995, ApJ, 451, 498
Netzer, H., et al. 2003, ApJ, 599, 933
Ogle, P. M., Marshall, H. L., Lee, J. C., & Canizares, C. R. 2000, ApJ, 545, L81
Peterson, B. M., et al. 2004, ApJ, 613, 682
Proga, D. 2003, ApJ, 592, L9
Proga, D., Stone, J. M., & Kallman, T. R. 2000, ApJ, 543, 686
Ramírez, J. M. 2008, A&A, 489, 57
Ramírez, J. M., Bautista, M., & Kallman, T. 2005, ApJ, 627, 166
Reeves, J. N., Nandra, K., George, I. M., Pounds, K. A., Turner, T. J., & Yaqoob, T. 2004, ApJ, 602, 648
Różańska, A., Goosmann, R., Dumont, A., & Czerny, B. 2006, A&A, 452, 1
Saez, C., Chartas, G., & Brandt, W. N. 2009, ApJ, 697, 194
Shields, J. C., & Hamann, F. 1997, ApJ, 481, 752
Shlosman, I., Vitello, P., & Mauche, C. W. 1996, ApJ, 461, 377
Steenbrugge, K. C., Kaastra, J. S., de Vries, C. P., & Edelson, R. 2003, A&A, 402, 477
Tarter, C. B., Tucker, W. H., & Salpeter, E. E. 1969, ApJ, 156, 943
Yaqoob, T., McKernan, B., Kraemer, S. B., Crenshaw, D. M., Gabel, J. R., George, I. M., & Turner, T. J. 2003, ApJ, 582, 105

J. M. Ramírez: Leibniz-Institut für Astrophysik Potsdam, An der Sternwarte 16, 14482 Potsdam, Germany (jramirez@aip.de).